Resonant Modes of Single Silicon Nanocavities Excited by Electron Irradiation

Toon Coenen,[†] Jorik van de Groep,[†,*] and Albert Polman

Center for Nanophotonics, FOM Institute AMOLF, Science Park 104, 1098 XG Amsterdam, The Netherlands, [†]These authors contributed equally to this work.

ABSTRACT High-index dielectric or semiconductor nanoparticles support strong Mie-like geometrical resonances in the visible spectral range. We use 30 keV angle-resolved cathodoluminescence imaging spectroscopy to excite and detect these resonant modes in single silicon nanocylinders with diameters ranging from 60 to 350 nm. Resonances are observed with wavelengths in the range of 400–700 nm, with quality factors in the range $Q = 9–77$, and show a strong red shift with increasing cylinder diameter. The photonic wave function of all modes is determined at deep-subwavelength resolution and shows good correspondence with numerical simulations. An analytical model is developed that describes the resonant Mie-like optical eigenmodes in the silicon cylinders using an effective index of a slab waveguide mode. It shows good overall agreement with the experimental results and enables qualification of all resonances with azimuthal ($m = 0–4$) and radial ($q = 1–4$) quantum numbers. The single resonant Si nanocylinders show characteristic angular radiation distributions in agreement with the modal symmetry.

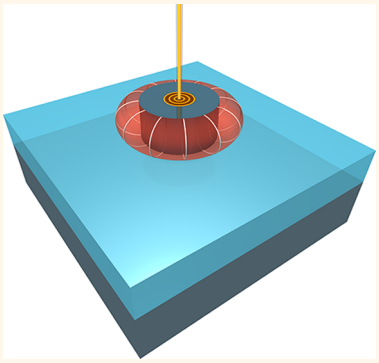

KEYWORDS: cavity · nanoantennas · dielectric · cathodoluminescence spectroscopy · Mie resonance · point dipole emitter · electron beam · silicon photonics · Fourier microscopy

Nanoparticles and nanowires made from high-index semiconductor or dielectric materials have the ability to strongly confine and scatter light.[1–4] These properties make them interesting for a large range of applications including solar cells,[5–14] lasers,[15] and nanoscale photodetectors or sensors.[16–20] Unlike their metallic counterparts, where light is confined to the surface in the form of surface plasmons, in semiconductor/dielectric nanostructures, light is mostly confined within the nanostructure. The resonant eigenmodes of these cavities are often referred to as Mie resonances, after the Lorentz–Mie–Debye solution to Maxwell's equations, which can be used to describe scattering by wavelength-scale spherical nanoparticles in a uniform dielectric environment.[1] They can also be referred to as geometrical resonances because of their similarity to whispering gallery modes.[7,21]

Silicon is an ideal base material for resonant Mie cavities. Due to its high refractive index, it can strongly confine light, while its indirect electronic band gap leads to relatively low absorption losses. Due to the compatibility with CMOS fabrication processes, resonant Si Mie scatterers can be readily integrated into optoelectronic devices based on silicon. The first applications of silicon Mie scatterers in metamaterials,[22–24] optical antennas,[2,22,25–27] and anti-reflection coatings[2] are appearing just recently and show the great potential of Mie scatterers as optical building blocks in nanophotonic nanostructures and devices. To fully unleash the potential of these nanoscale Si light scatterers, detailed understanding of their fundamental scattering properties is essential. However, standard optical techniques have been unable to fully resolve the Mie resonant modes due to lack of spatial resolution.

In this article, we study the resonant optical properties of individual silicon cylinders using angle-resolved cathodoluminescence (CL) imaging spectroscopy.[28–30] With this technique, a 30 keV electron beam acts as a broad-band point source of light that can be employed to probe the optical properties of nanostructures with deep-subwavelength spatial resolution.[31,32] We determine the spectral and

* Address correspondence to groep@amolf.nl.

Received for review December 10, 2012 and accepted January 11, 2013.

Published online January 12, 2013
10.1021/nn3056862

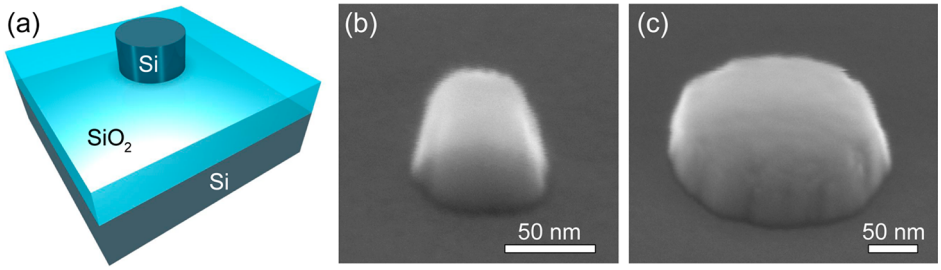

Figure 1. (a) Sketch of the sample geometry. Single silicon cylinders are positioned on a silica layer, supported by a silicon substrate. SEM images of fabricated cylinders with base diameters of (b) 80 nm and (c) 200 nm. The cylinders are slightly tapered toward the surface.

spatial characteristics of the resonant optical eigenmodes for single silicon nanocylinders with different diameters. We compare our results with finite-difference time-domain (FDTD) simulations and an analytical model, and we identify the fundamental and higher-order radial and azimuthal modes of the cavities. In addition, we present experimental data on the angular distribution and polarization of light emission from single resonant Mie cavities.

RESULTS AND DISCUSSION

Sample Fabrication. Figure 1a shows the geometry of the sample. Single Si nanocylinders were fabricated on a thin SiO_2 layer, supported by a Si substrate. The fabrication starts with a silicon-on-insulator (SOI) wafer with a 100 nm Si layer on a 300 nm SiO_2 layer. Electron beam lithography (EBL) is used to write circular pads as an etch mask in a negative tone resist. Next, anisotropic reactive ion etching (RIE) is used to etch down the top Si layer of the SOI wafer, such that Si nanocylinders are formed on top of the silica layer. Residual resist is removed using an oxygen plasma etch. The resulting cylinders have diameters ranging from 60 to 325 nm and are 100 nm high. Scanning electron micrographs of a small (d = 80 nm) and large (d = 200 nm) cylinder are shown in Figure 1b,c, respectively. From the electron micrographs, it can be seen that the cylinders are slightly tapered due to the nonperfect anisotropy of the Si etch but clearly resemble the intended cylindrical structure.

Experiment. To measure the resonant optical properties of single cylinders, we use angle-resolved cathodoluminescence (CL) imaging spectroscopy.[28−30] The electric field generated by a high-energy electron passing through a dielectric nanoparticle induces a transient vertically oriented polarization that results in the coherent excitation of the resonant modes supported by the Si nanocylinder at a rate that is proportional to the out-of-plane component of the local density of optical states (LDOS).[31,32] The excited local modes radiate into the far field; the radiation is collected by a parabolic mirror placed between the sample and the electron column, after which both the spectrum and the angular distribution are analyzed. Since the electron beam can be scanned at very high spatial resolution and the electron range is well beyond the thickness of the Si nanostructures, spatial information about the optical modes inside the nanostructures can be obtained far below the diffraction limit of light.

To probe the resonant optical response we raster-scan a 30 keV electron beam in 10 nm steps over a Si cylinder and collect a CL spectrum for each position. In parallel, we collect the secondary electron (SE) signal to obtain geometrical information about the cylinder (see insets in Figure 2a,b). These data are used to define a spatial mask for the CL data, based on a threshold in SE counts, in order to select the pixels in the CL map corresponding to the Si cylinder.

The CL from the Si cylinders is superimposed on a broad background signal peaking at λ_0 = 650 nm due to CL from intrinsic defects in the SiO_2 matrix, which can vary slightly in intensity over time under electron beam illumination.[33] We use a triangular interpolation routine to subtract this variable background from the CL signal from the cylinders (see Methods section). In the experimental geometry, the thickness of the SiO_2 layer was chosen as a compromise between minimizing background from the SiO_2 layer on the one hand and optical isolation of the Si cylinder from the high-index silicon substrate on the other hand.

Figure 2a shows the spatially integrated CL spectrum for an 82 nm diameter nanocylinder. A clear peak is observed in the spectrum at λ_0 = 439 nm corresponding to an optical resonance in the nanoparticle. For accurate determination of the peak wavelength, we fit a Lorentzian line shape to the spectrum, using a least-squares fitting routine (solid gray curve). From the width of the Lorentzian, we determine the quality factor of the resonance to be Q = 6. The magnitude of Q is determined both by absorption of light by the Si cylinder and radiative loss. Figure 2b shows the CL spectrum for a 321 nm diameter cylinder, which shows multiple peaks at λ_0 = 440, 480, 515, 578, and 662 nm (labeled 2−6 in the figure, as will be discussed further on). Due to the larger diameter, this cylinder supports multiple resonant modes of different order within the experimental spectral range. The spectrum is fitted with a sum of five Lorentzians (black curve) which corresponds well to the measured spectrum. The quality

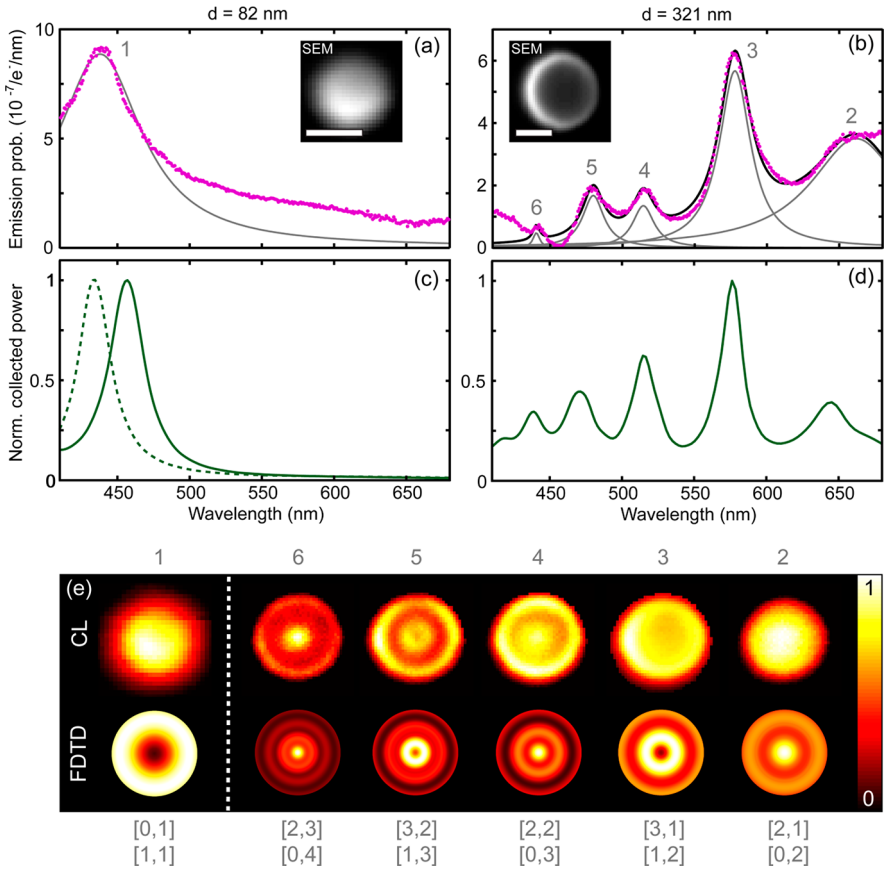

Figure 2. (a) Spatially integrated cathodoluminescence spectrum (purple dots) for an 82 nm diameter cylinder. A Lorentzian line shape is fitted to the spectrum (gray curve). The inset shows the secondary electron map collected simultaneously with the CL data collection (scale bar: 50 nm). (b) Similar measurement for a 321 nm diameter particle. The spectrum is fitted with a sum of five Lorentzians (black curve) that are also plotted individually (scale bar SEM image: 150 nm). (c) Normalized FDTD simulation of collected power as function of wavelength for 80 nm (solid green curve) and 70 nm (dashed green curve) cylinders. (d) Same as (c) for a 321 nm cylinder (solid green curve). (e, Top row) Two-dimensional CL intensity maps shown at resonance wavelengths indicated in (a) and (b), displaying the photonic wave functions of the different resonances. (e, Bottom row) Corresponding time-averaged intensity maps calculated using FDTD. The labels [*m*,*q*] indicate the corresponding branches in Figure 3b from the analytical model.

factors derived from the individual fits are $Q = 77$, 27, 29, 22, and 9 for modes with increasing wavelength. Note that the high quality factor of the first peak at $\lambda_0 =$ 440 nm has a large uncertainty due to the low intensity with respect to the background signal. To study the spatial characteristics (*i.e.*, the "photonic wave functions" of the resonant modes), we determined the two-dimensional excitation distribution at each resonance wavelength. To obtain sufficient signal-to-noise ratio, we integrate the spectra over a 20 nm bandwidth. Figure 2e (top row) shows these maps for the numbered peak wavelengths indicated in Figure 2a,b. For the small nanoparticle, the CL emission is observed from the entire nanoparticle, with an antinode (maximum) observed in the center. For the large cylinder, the spatial maps are more complex and consist of multiple rings and dots with alternating minima and maxima in the center, corresponding to resonances with higher radial mode orders, as will be discussed below.

Numerical Modeling. Numerical modeling is performed using finite-difference time-domain (FDTD) simulations.[34] Single Si cylinders (diameter $d = 50-350$ nm, height $h =$ 100 nm) are placed on a 300 nm thick SiO_2 layer on a Si substrate. In the simulations, the electron source is approximated by a single broad-band vertically oriented electric dipole positioned at 50 nm height inside the cylinder. Radiation from the cylinder into the upper hemisphere is collected using transmission monitors. To simulate a resonant spectrum, the dipole position is varied from the center ($r = 0$) to the outer radius of the cylinder ($r = d/2$), in steps of 5 nm. The collected power spectrum for each radius is then multiplied by $2\pi r$ to account for the cylindrical geometry; all power spectra are summed, and the result is normalized to its maximum. Optical constants for Si and SiO_2 are taken from Palik.[35]

The results for the 80 and 320 nm diameter cylinders are shown in Figure 2c,d, respectively, where the spatially integrated collected power (green solid lines) is shown as a function of free space wavelength. As in the experiment, the 80 nm cylinder clearly shows one single peak ($Q = 16$), corresponding to the lowest-order

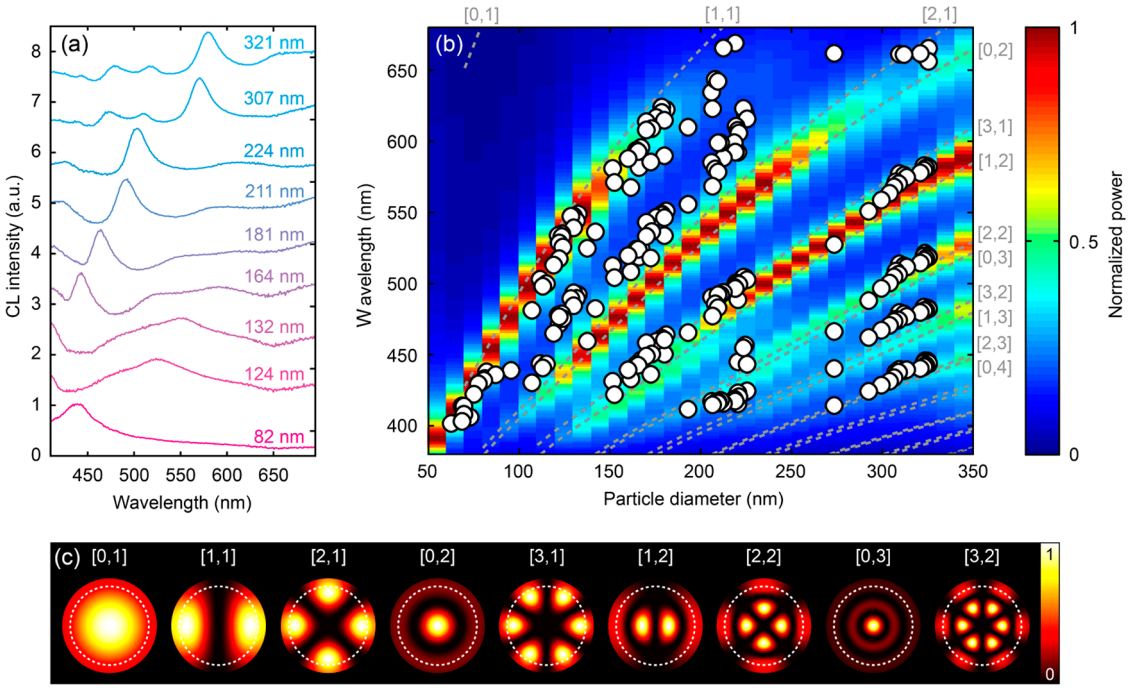

Figure 3. (a) Spatially integrated CL spectra for different cylinder diameters. The normalized spectra have been vertically offset for clarity. All resonances show a clear red shift for larger diameters. (b) Resonance peak wavelengths for different cylinder diameters obtained by fitting the CL spectra with Lorentzians (white dots). The color map shows the emitted power as function of particle diameter and wavelength, calculated using FDTD (normalized to its maximum for each particle diameter). The dashed gray curves correspond to the eigenvalues found for different diameter cylinders using the analytical 2D disk resonator model. Each curve is associated with a particular radial and azimuthal quantum number, indicated by the [*m*,*q*] notations on the top and side of the figure. (c) Photonic wave functions for a d = 320 nm cylinder obtained from the analytical model. The time-averaged amplitude $|E_z(r,\varphi)|^2$ is plotted. The white dashed circles indicate the edge of the particle.

resonance, whereas the 320 nm cylinder shows many peaks due to higher-order resonances. Compared with the experiment for the 80 nm cylinder, the simulated peak wavelength is off by 18 nm. We attribute this to the small tapering of the cylinders, resulting in a slightly reduced diameter at the surface, as can be observed in Figure 1b,c. Indeed, the simulated spectrum for a 70 nm diameter (dashed line) matches the measured spectrum quite well. This indicates that the effective diameter of a particle with an 80 nm diameter base is 70 nm, in good correspondence with the SEM image in Figure 2a. The simulated spectrum for the 320 nm diameter particle in Figure 2d shows good agreement with the different resonances with the experiment. In agreement with the experiment, the simulated peak at λ_0 = 575 nm has the highest intensity. The simulated quality factor for the five modes is Q = 21, 19, 24, 30, and 15, which is in the same range as the experimental values, except for the small lowest-wavelength peak. The observed Q is determined by both absorption in the particle and the radiative coupling to the far field. Absorption losses are larger in the blue spectral range due the higher absorption of silicon in that wavelength range.

Figure 2e, bottom row, shows the simulated time-averaged photonic wave functions. Analogous to the experiment, the peak intensity is integrated over a 20 nm bandwidth around the peak wavelength for each dipole position, giving the peak intensity as a function of radial position. The data set is then rotated to obtain the two-dimensional photonic wave function maps. Simulations are shown for the 80 and 320 nm diameter cylinders for each resonance. The simulated photonic wave function of the lowest-order mode for the 82 nm cylinder (peak 1) shows a bright ring, while the measurement shows a more uniform distribution peaking in the center. For the 320 nm cylinder, the simulations show good agreement with the measured trends. For lower resonance wavelengths (going from peak 2 to peak 6), more nodes and antinodes are observed in the radial direction, corresponding to higher-order radial modes. For the highest-order mode (peak 6), a bright dot is observed in the center, surrounded by two bright rings. The alternating dark and bright center of the cylinder observed for subsequent resonances is also reproduced in the simulations.

Mode Evolution as a Function of Particle Diameter. From Figure 2, it is clear that the resonant behavior of the cylinders strongly depends on the diameter. To gain more insight into the spectral mode evolution of the resonances for different sizes, we collected the CL spectra from 88 different cylinders with diameters ranging from 60 to 325 nm. Figure 3a shows a representative subset of this data set with spectra for different diameters. As the diameter increases, higher-order resonances emerge and all resonances

progressively red shift as is expected for geometrical resonances.[1]

By using the Lorentzian fitting shown in Figure 2a,b, we determined the resonance peak wavelength for all measured cylinders. In Figure 3b, these peak wavelengths are shown as a function of diameter. This figure clearly shows how each resonance mode gradually red shifts for increasing diameter. To compare the experimental resonances with the results from numerical modeling, we also plot the collected power as a function of diameter and wavelength in a 2D color plot (Figure 3b). Here, every vertical slice in the color plot corresponds to a normalized spectrum, as shown in Figure 2c,d. The FDTD simulations show multiple branches, each of which corresponds to a particular resonant mode in the cylinders. Both the number of peaks as well as their peak wavelength show good agreement with the measurements, except the second branch from the top, for which the simulation is blue-shifted with respect to the measurements.

To study the nature of these resonances in more detail, we developed an analytical 2D disc resonator model.[36−40] In this model, we solve for the cylindrical modes of an infinitely long cylinder, which can be analytically calculated using Maxwell's equations. Confinement in the normal direction is then included using a planar waveguide model. This is a reasonable assumption for cylinders with a diameter (much) larger than the thickness. Figure 4a shows the 2D slab waveguide geometry with the Si/SiO_2/Si layer stack. The 100 nm thin Si slab supports both a fundamental transverse electric (TE_0) and transverse magnetic (TM_0) mode. The incoming electrons mainly couple to vertical electric field (E_z) and in-plane transverse magnetic field components (H_T),[31] which both match the field orientations of the TM mode (see Figure 4a), so that only this mode is considered further. We use a numerical method to solve for the dispersion curve of the TM_0 mode and derive from it the mode index n_{eff} at each wavelength. The result is shown in Figure 4b (magenta), along with the refractive index of Si (cyan), SiO_2 (red), and air (black dashed line). For reference, the effective mode index of the TE_0 mode is also shown (blue). Figure 4b shows that the effective index of the TM_0 mode gradually decreases from a value close to that of Si at short wavelengths to an index approaching that of SiO_2 for long wavelengths. This can be understood from the increasing overlap of the evanescent tail of the mode profile with the silica and air cladding layer, as the wavelength is increased. We now use this effective index of the Si slab modes as input for the index of the cylinder[38−40] in the 2D Helmholtz wave equation[36,37]

$$(\nabla_T + n^2 k_0^2 - \beta^2)\Psi = 0 \qquad (1)$$

to solve for the radial modes. Here, Ψ is the wave function of the out-of-plane field, ∇_T is the transverse

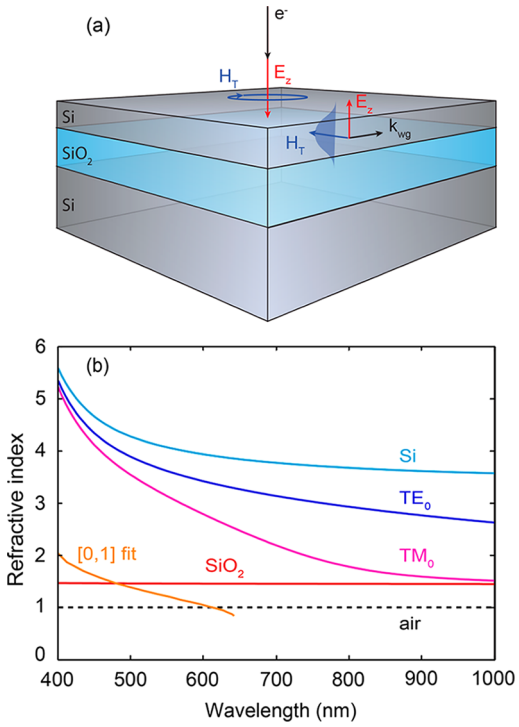

Figure 4. (a) Sketch of the layer structure used in the 2D analytical model to calculate the effective mode index of the TM_0 waveguide mode. Also shown are the electromagnetic field components induced by an incoming electron and those of the TM_0 waveguide mode. (b) Real part of the (effective) refractive index of the TM_0 mode (magenta), compared with the index of bulk Si (cyan curve), SiO_2 (red curve), air (dashed black curve), and the TE_0 mode (blue curve). The orange line shows the index obtained when fitting the $m = 0$, $q = 1$ mode to the top resonance branch obtained from numerical modeling. It shows a cutoff above $\lambda = 620$ nm.

gradient, n is the refractive index in the medium, k_0 is the free space wave vector, and β is the propagation constant in the vertical direction. The solution for eq 1 is given by

$$\Psi(r,\phi) = \begin{cases} a\dfrac{J_m(\sqrt{n_c^2 k_0^2 - \beta^2} r)}{J_m(\sqrt{n_c^2 k_0^2 - \beta^2} R)} e^{im\phi} & 0 < r < R \\ b\dfrac{K_m(\sqrt{\beta^2 - n_s^2 k_0^2} r)}{K_m(\sqrt{\beta^2 - n_s^2 k_0^2} R)} e^{im\phi} & R < r < \infty \end{cases} \qquad (2)$$

Here, a and b are constants, J_m is the Bessel function of the first kind, K_m is the modified Bessel function of the second kind, m is the azimuthal mode number, n_c is the effective refractive index of the cylinder, n_s the refractive index of the surrounding medium (vacuum), r the radial position, φ the azimuthal angle, and R the radius of the cylinder. We consider the 2D solutions for the TM modes, $\beta = 0$ and $\Psi = E_z$. The transverse field components can easily be derived from eq 2.[36,37] The eigenvalue equation can be obtained from eq 2 by applying the boundary conditions $E_{z,c}(R) = E_{z,s}(R)$ and

$H_{\varphi,c}(R) = H_{\varphi,s}(R)$ (c = cylinder, s = surrounding), which can then be solved for different particle radii to give the eigenvalues, corresponding to the resonance wavelengths. For a given azimuthal mode number m (where $m = 0, \pm1, \pm2, \ldots$ and $m = \pm i$ are degenerate), multiple solutions are found. These correspond to higher-order resonances in the radial direction, with radial mode numbers $q = 1, 2, \ldots$.

Resonant modes calculated using the above model are shown in Figure 3 as gray dashed lines. The quantum numbers $[m,q]$ of each branch are indicated on the top and side of the graph, with the lowest-order mode [0,1] occurring for the longest wavelengths. The corresponding mode profiles $|E_z(r,\varphi)|^2$ are shown in Figure 3c for the first nine branches, where the dashed white circle indicates the edge of the cylinders. These mode maps also show the azimuthal variations in the photonic wave functions that remain unobserved in the experiment, due to the cylindrical symmetry of the nanoparticle. The model shows good qualitative agreement with the measured data (white dots) and the numerical modeling (colormap); that is, experimental and numerical modal branches each lie close to one or two calculated branches. By comparing the model with the experimental and numerical data, we gain several insights.

First, the increasing number of peaks with increasing diameter observed in Figure 3a,b reflects the excitation of higher-order resonances. When increasing the particle diameter at a fixed wavelength, both the azimuthal (m) and the radial (q) mode orders increase stepwise. In particular, for the higher-order resonances, the analytically calculated resonances match well with the numerically calculated ones. For example, the [2,1] and [0,2] branches that could not be resolved experimentally show a close match between the analytical model and numerical simulations.

Second, we can now label the complex photonic wave function maps observed in Figure 2e as a superposition of the two photonic wave functions corresponding to the resonances that match the FDTD branches in Figure 3b. For example, the [3,1] and [1,2] modes in Figure 3c together correspond to the map of peak 3 in Figure 2e, with a dark center and two bright rings. The eigenmodes assigned to the simulated profiles in Figure 2e are indicated at the bottom of that figure. The good correspondence between experiment, numerical model, and analytical model is also reflected by the fact that for the 320 nm diameter disc only those with an azimuthal order $m = 0$ show an antinode in the center (peaks 2, 4, and 6).

Third, the analytically calculated modes show strong dispersion (curved resonance branches), in agreement with both the measurements and the FDTD data. This originates from the dispersive effective refractive index n_c of the cylinder due to the strong modal confinement in the vertical dimension. Indeed, the strongly decreasing index as a function of wavelength, as observed in Figure 4b for the TM_0 mode proves to be essential to predict the shape of the measured and FDTD simulated resonance branches. In fact, if the cylinder would be described using the (dispersive) index of bulk Si or using the TE_0 mode, the analytically calculated modal branches in Figure 3b would increase superlinearly rather than sublinearly for longer wavelengths as is observed in the experiment and FDTD simulations. This directly proves that the modal dispersion due to the vertical confinement strongly influences the resonant behavior.

While the analytical model thus predicts many of the key features and trends in both the experiments and FDTD simulations, one discrepancy is observed: the calculated lowest-order resonance [0,1], which is visible in the top left corner of Figure 3b, does not match with any branch observed in the experiment or simulations. This implies that either the lowest-order resonance is not excited in the experiment or that the assumptions of the simple 2D analytical model break down in the range where the wavelength is large compared to the particle diameter. Indeed, the waveguide model assumes an infinitely wide disk.

To resolve this issue, we measured the angular emission profiles of individual Si cylinders in the CL system.[28] Here, the light radiated by the cylinders is collected by the parabolic mirror and projected onto a CCD imaging camera; each pixel corresponds to a unique azimuthal/zenithal angle. Using this technique, it is possible to determine the angular emission properties for such a 3D structure on a layered substrate, which is difficult if not impossible to predict either analytically or with numerical methods such as the boundary element method (BEM), FDTD, or finite-element methods (FEM).

Figure 5 shows the measured radiation patterns for four different cylinders measured on different resonance branches in Figure 3b. The pattern strongly depends on the resonance mode order. For the smallest cylinder (Figure 5a), which has a resonance lying on the top experimental branch in Figure 3b, we observe a toroidal "doughnut-like" emission pattern at $\lambda_0 =$ 400 nm, which has no light emission along the normal.[29,41−43] This pattern corresponds to that of a vertically oriented dipole [0,1] mode, which directly proves that the top measured branch corresponds to the [0,1] branch. Note that the [1,1] mode is not excited in the angular CL experiment as the cylinders are excited in the center, where the [1,1] mode has a node (see Figure 3c). We explain the large discrepancy between the experimentally observed top branch and the analytically calculated [0,1] mode by the fact that the analytical waveguide model breaks down when the diameter is small compared to the wavelength. With the experimental data for the top branch in Figure 3b, identified as the [0,1] mode, we conclude

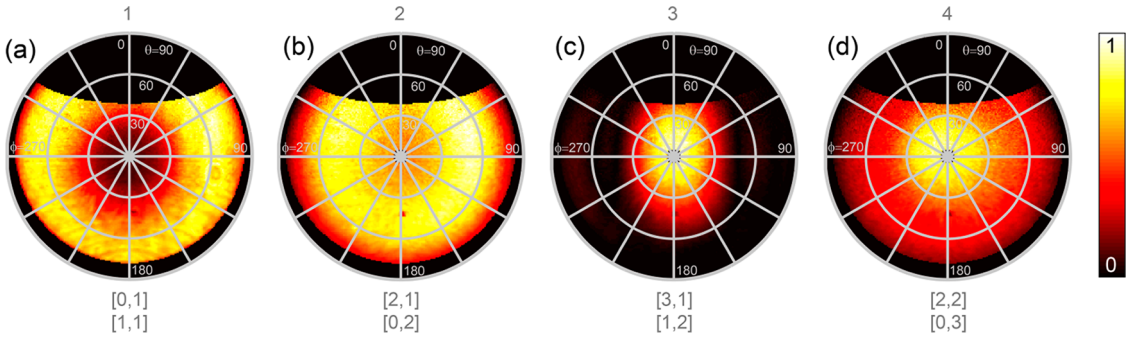

Figure 5. Measured angular patterns for the first four modal branches showing the CL emission intensity as function of zenithal angle θ and azimuthal angle φ for (a) $d = 70$ nm, (b) $d = 153$ nm, (c) $d = 176$ nm, and (d) $d = 304$ nm collected at $\lambda_0 = 400$, 500, 450, and 500 nm, respectively. The specific diameters were chosen to optimally match a band-pass color filter. For all of the images, the cylinders were excited in the center, except for (c), where the cylinder was excited at the edge to optimize the excitation efficiency since this resonance has a node in the center.

that the [0,1] and [1,1] modal branches are closely spaced and overlap with the top experimental branch, as in the case for all other experimental branches, which also correspond to combinations of two modes (see Figure 3b).

The angular profile for the second branch (Figure 5b) shows a toroidal shape, as well, consistent with the electron beam selectively exciting the [0,2] mode (the [2,1] mode has a node in the center; see Figure 3c), which also has a vertical dipole moment. The modes in the third branch cannot be excited in the center ($m > 0$ for both modes), and therefore, the beam was placed on the edge of the cylinder, exciting a superposition of the [1,2] and [3,1] modes. In this case, clear upward beaming is observed, in agreement with the in-plane character of this mode (see Figure 3c). The angular pattern for the fourth branch (Figure 5d) appears to be a combination of a toroidal and upward emission. This corresponds to the excitation of the toroidally emitting [0,3] mode and a small contribution of the upward radiating [2,2] quadrupolar mode; while the latter has a node in the center, given the close proximity of its first radial antinode to the center (see Figure 3c), it can be excited by the finite-size electron beam.

The large difference in radiation profile between the resonance orders shows that, depending on the angular scattering profile that is desired for specific applications, the cylinder geometry can be tuned to obtain such a scattering profile in the appropriate spectral range. Note that the angular distribution is also influenced by the wavelength-dependent interference with the silicon substrate 300 nm below the nanoparticle.[32,43]

To investigate whether the lowest-order [0,1] dipolar resonance is electric or magnetic in nature,[22,24−27] we perform polarization-filtered angular measurements, using a linear polarizer in the beam path. Figure 6 shows the angular pattern with the polarizer parallel (a) and transverse (b) to the optical axis of the paraboloid (see blue dashed lines) for the smallest cylinder ($d = 70$ nm) at $\lambda_0 = 400$ nm. In the paraboloid, the emission

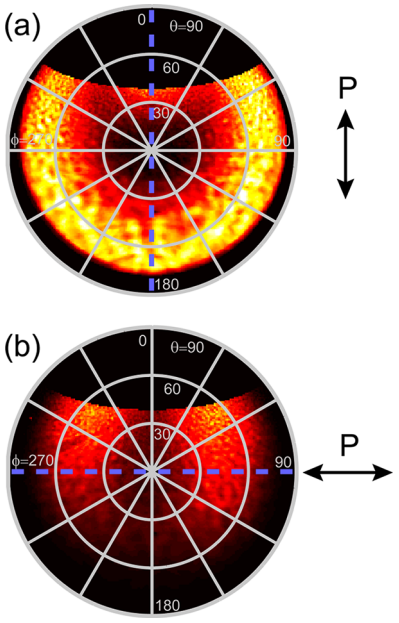

Figure 6. Measured polarization-filtered angular patterns for a $d = 70$ nm cylinder measured at $\lambda_0 = 400$ nm with the polarizer positioned (a) vertically (aligned with the optical axis of the paraboloid) and (b) horizontally (transverse to the optical axis). The patterns suggest that this resonance is an electrical dipolar $m = 0$, $q = 1$ resonance.

polarization remains almost unaltered along the center line of the mirror (the line going through $\varphi = 0$ and 180°). We observe that the light intensity is high along this line when the polarizer is aligned, while it is low when it is transversely oriented. This indicates that the emission is p-polarized, which is consistent with the radiation from an $m = 0$, $q = 1$ electric dipole mode. For a more elaborate description on why these polarization-filtered angular patterns have this specific shape and how the parabolic mirror affects the emission polarization for different electric dipole orientations, we refer the reader to ref 30.

Finally, we use the knowledge that the upper experimental/numerical branch corresponds to a [0,1] resonance to fit its appropriate effective index. To do this, we again solve the eigenvalue equation, but now

we fix the resonance wavelength to the resonance wavelengths obtained for the top branch from numerical modeling and solve for n_c, given that $m = 0$ and $q = 1$. In this way, we force the [0,1] branch of the model to match the experimental data and use this to obtain the effective index of the cylinder. The resulting index is shown as an orange line in Figure 4b and is indeed significantly lower than the TM_0 index that was originally used and gives rise to a significant blue shift of the resonance wavelength. The fitted index steadily decreases with increasing wavelength from $n = 2.0$ at $\lambda_0 = 400$ nm to $n < 1$ for $\lambda_0 > 620$ nm. This implies that the lowest-order resonance approaches cutoff and becomes a leaky mode that no longer strongly confines light inside the cavity. Close observation of Figure 3b shows that both the experimental and simulation data of the top resonance branch fade away around this wavelength, in agreement with this cutoff argument. We note that the decrease in effective mode index for the cutoff mode with increasing wavelength is due to both the reduced confinement and the lower index of bulk silicon at larger wavelengths. The strong reduction in Q for the [0,1] mode with increasing diameter is also clearly visible in Figure 3a.

CONCLUSION

In conclusion, the resonant optical modes of silicon nanocylinders with diameters between 60 and 325 nm can be excited and studied using a 30 keV electron beam. Well-defined fundamental and higher-order azimuthal ($m = 0-4$) and radial ($q = 1-4$) modes are observed with relatively narrow ($Q = 9-77$) emission peaks and complex photonic wave functions. The data agree with finite-difference time-domain simulations and analytical calculations, in which we solve the Helmholtz wave equation using an effective modal index for the corresponding TM_0 waveguide mode to find the in-plane eigenmodes. Characteristic angular emission patterns are observed for each resonant mode, ranging from an upward dipole-like pattern for the lowest-order modes to distributions that show clear beaming in the upward direction for higher-order modes. Using polarization spectroscopy, we identify the lowest-order resonance as an ($m = 0$, $q = 1$) electrical dipole mode; it becomes leaky for long wavelengths.

Our measurements demonstrate that the optical properties of silicon nanocylinders are highly tunable through the visible spectral range. Further tunability may be achieved by varying the nanoparticle shape. With the fundamental resonant optical properties of single Si Mie resonators now determined, the door is open to studies of more complex geometries of arrays of coupled resonators, in which the directionality and spectra of emitted light can be tuned further. This work also shows that cathodoluminescence spectroscopy, which so far has been used mostly on resonant metallic nanostructures, can be used to study the fundamental resonant properties of single dielectric or semiconductor nanostructures in great detail. In the future, this enables rapid prototyping of semiconductor or dielectric nanostructures, where the spectral and angular emission properties can be fine-tuned for specific applications.

METHODS

Fabrication. Small chips (12 × 12 mm) of SOI wafer (100 nm Si device layer, 300 nm SiO_2 buried oxide layer) are baked for 5 min at 180 °C before spin coating the sample with a thin HMDS adhesion layer (4000 rpm, 30 s). The HMDS layer is baked for 1 min at 180 °C to evaporate the solvents. Next, the sample is spin coated with approximately 65 nm of negative tone resist (ma-N 2401, 2000 rpm, 30 s) and baked for 60 s at 90 °C. Au colloids with a diameter of 50 nm are deposited in the corner of the sample to allow accurate focusing of the electron beam.

Electron beam lithography is performed in a Raith e-LINE system, using a 30 kV acceleration voltage and 7.5 μm aperture, resulting in a beam current of 14 pA. Single dot exposure is used for the smallest cylinders ($d < 240$ nm), whereas area exposure is used for the larger cylinders ($d > 270$ nm). The resist is developed by rinsing in ma-D 332 S for 15 s, followed by rinsing in deionized H_2O to stop the development.

The resulting disks of resist function as an etch mask in the reactive ion etching (RIE) step. A gas mixture of CHF_3 (35 sccm) and SF_6 (5 sccm) is used to anisotropically etch down the Si layer of the SOI wafer (100 nm) in 3.5 min (forward power = 125 W). Subsequently, the residual resist is removed using a 10 min oxygen plasma etch (20 sccm O_2, 50 W forward power).

CL Experiment. The CL experiment was performed in a FEI XL-30 SFEG scanning electron microscope with an aluminum parabolic mirror inside. The mirror alignment is performed using a specially designed piezoelectric positioning system.[29] For spectral imaging, the CL was focused onto a fiber connected to a spectrometer with a liquid-nitrogen-cooled CCD array. For the angular measurements, the CL beam was projected onto a 1024 × 1024 pixel imaging CCD array. Emission patterns were obtained by mapping the 2D CCD image of the CL beam onto emission angle θ (zenithal angle) and φ (azimuthal angle) and correcting for the collected solid angle per CCD pixel.[28] For the spectral images, 0.3 s integration time per pixel was used at a current of 10 nA. We use a spatial drift correction algorithm to correct for the effects of beam and sample drift. The data are corrected for system response using a measured transition radiation spectrum from gold and comparing that to theory,[31,44] so that the absolute excitation efficiency is determined per electron per unit bandwidth. For the angle-resolved measurements, we used dwell times between 15 and 30 s depending on wavelength. For the polarization-filtered angular measurements, we used an integration time of 60 s. Spectral sensitivity was achieved by filtering the CL beam with 40 nm band-pass color filters. In all cases, the background CL signal from the substrate was subtracted from the measured data, which includes the transition radiation of the SiO_2 layer and Si substrate. To correctly subtract the variable background from the CL signal, we use a triangular interpolation routine, which interpolates the background intensity between the four corners (averaged over nine pixels in each corner) of the scan.

FDTD Simulations. The finite-difference time-domain simulations are performed using the commercial software package Lumerical FDTD Solutions.[34] An 800 nm cubed simulation box is used, with perfectly matching layer (PML) boundary conditions

on all sides. The simulation box ranges from 150 nm into the Si substrate to 250 nm above the top of the cylinders. A constant-current broad band (λ_0 = 300−900 nm) vertically oriented electric dipole, positioned at half the height of the cylinder (50 nm), is used as a source. To simulate the spectrum for a given cylinder diameter, the dipole position is varied from the center to the edge of the cylinder in steps of 5 nm, such that the number of simulations N per cylinder is given by $N = R/5 + 1$, with R being the particle radius in nanometers. Two-dimensional flux box transmission monitors, the top one positioned 100 nm above the top interface of the cylinder, the side ones 360 nm from the center of the cylinder, monitor the power of the light emitted into the upper hemisphere. Note that interference with the Si substrate is taken into account, but that light reflected from the SiO_2−Si interface under large angles may be radiated into the upper hemisphere without being detected. Automatic non-uniform meshing is used, resulting in mesh sizes ranging from 4 to 7 nm in the Si cylinder or air, respectively.

Conflict of Interest: The authors declare no competing financial interest.

Acknowledgment. We would like to acknowledge Femius Koenderink for useful discussions, and Sander Mann, Erik Garnett, and Benjamin Brenny for careful reading of the manuscript. This work is part of the research program of the "Stichting voor Fundamenteel Onderzoek der Materie (FOM)", which is financially supported by the "Nederlandse Organisatie voor Wetenschappelijk Onderzoek (NWO)". This work was funded by an ERC Advanced Investigator Grant and is also part of NanoNextNL, a nanotechnology program funded by the Dutch ministry of economic affairs.

REFERENCES AND NOTES

1. Bohren, C. F.; Huffman, D. R. *Absorption and Scattering of Light by Small Particles*; John Wiley & Sons: New York, 1983.
2. Schuller, A. J.; Brongersma, M. L. General Properties of Dielectric Optical Antennas. *Opt. Express* **2009**, *17*, 24084–24095.
3. Sainidou, R.; Renger, J.; Teperik, T. V.; González, M. U.; Quidant, R.; García de Abajo, F. J. Extraordinary All-Dielectric Light Enhancement over Large Volumes. *Nano Lett.* **2010**, *10*, 4450–4455.
4. Grzela, G.; Hourlier, D.; Gómez Rivas, J. Polarization-Dependent Light Extinction in Ensembles of Polydisperse Vertical Semiconductor Nanowires: A Mie Scattering Effective Medium. *Phys. Rev. B* **2012**, *86*, 045305.
5. Spinelli, P.; Verschuuren, M. A.; Polman, A. Broadband Omnidirectional Antireflection Coating Based on Subwavelength Surface Mie Resonators. *Nat. Commun.* **2012**, *3*, 692.
6. Kelzenberg, M. D.; Boettcher, S. W.; Petykiewicz, J. A.; Turner-Evans, D. B.; Putnam, M. C.; Warren, E. L.; Spurgeon, J. M.; Briggs, R. M.; Lewis, N. S.; Atwater, H. A. Enhanced absorption and carrier collection in Si wire arrays for photovoltaic applications. *Nat. Mat.* **2010**, *9*, 239−244.
7. Grandidier, J.; Callahan, D. M.; Munday, J. N.; Atwater, H. A. Light Absorption Enhancement in Thin-Film Solar Cells Using Whispering Gallery Modes in Dielectric Nanospheres. *Adv. Mater.* **2011**, *23*, 1272–1276.
8. Raman, A.; Yu, Z.; Fan, S. Dielectric Nanostructures for Broadband Light Trapping in Organic Solar Cells. *Opt. Express* **2011**, *19*, 19015–19026.
9. Mann, S.; Grote, R. R.; Osgood, R. M.; Schuller, J. A. Dielectric Particle and Void Resonators for Thin Film Solar Cell Textures. *Opt. Express* **2011**, *19*, 25729–25740.
10. Kim, S.; Day, R. W.; Cahoon, J. F.; Kempa, T. J.; Song, K.; Park, H.; Lieber, C. M. Tuning Light Absorption in Core/Shell Silicon Nanowire Photovoltaic Devices through Morphological Design. *Nano Lett.* **2012**, *12*, 4971–4976.
11. Yu, Y.; Ferry, V. E.; Alivisatos, A. P.; Cao, L. Dielectric Core−Shell Optical Antennas for Strong Solar Absorption Enhancement. *Nano Lett.* **2012**, *12*, 3674–3681.
12. Yao, Y.; Yao, J.; Narasimhan, V. K.; Ruan, Z.; Xie, C.; Fan, S.; Cui, Y. Broadband Light Management Using Low-*Q* Whispering Gallery Modes in Spherical Nanoshells. *Nat. Commun.* **2012**, *3*, 664.
13. Vasudev, A. P.; Schuller, A. J.; Brongersma, M. L. Nanophotonic Light Trapping with Patterned Transparent Conductive Oxides. *Opt. Express* **2012**, *20*, A385–A394.
14. Tang, J.; Huo, Z.; Brittman, S.; Gao, H.; Yang, P. Solution-Processed Core−Shell Nanowires for Efficient Photovoltaic Cells. *Nat. Nanotechnol.* **2011**, *6*, 568–572.
15. van de Molen, K. L.; Zijlstra, P.; Lagendijk, A.; Mosk, A. P. Laser Threshold of Mie Resonances. *Opt. Lett.* **2006**, *31*, 1432–1434.
16. Cao, L.; White, J. S.; Park, J. S.; Schuller, J. A.; Clemens, B. M.; Brongersma, M. L. Engineering Light Absorption in Semiconductor Nanowire Devices. *Nat. Mater.* **2009**, *8*, 643–647.
17. Cao, L.; Park, J.; Fan, P.; Clemens, B.; Brongersma, M. L. Resonant Germanium Nanoantenna Photodetectors. *Nano Lett.* **2010**, *10*, 1229–1233.
18. Alù, A.; Engheta, N. Cloaking a Sensor. *Phys. Rev. Lett.* **2009**, *102*, 233901.
19. Fan, P.; Chettiar, U. K.; Cao, L.; Afshinmanesh, F.; Engheta, N.; Brongersma, M. L. An Invisible Metal-Semiconductor Photodetector. *Nat. Photonics* **2012**, *6*, 380–385.
20. Yan, R.; Park, J.; Choi, Y.; Heo, C.; Yang, S.; Lee, L. P.; Yang, P. Nanowire-Based Single-Cell Endoscopy. *Nat. Nanotechnol.* **2011**, *7*, 191–196.
21. Kippenberg, T. J.; Vahala, K. J. Cavity Opto-Mechanics. In *Practical Applications of Microresonators in Optics and Photonics*; CRC Press: Boca Raton, FL, 2009.
22. García-Etxarri, A.; Gómez-Medina, R.; Froufe-Pérez, L. S.; López, C.; Chantada, L.; Scheffold, F.; Aizpurua, J.; Nieto-Vesperinas, M.; Sáenz, J. J. Strong Magnetic Response of Submicron Silicon Particles in the Infrared. *Opt. Express* **2011**, *6*, 4815–4826.
23. Zhao, Q.; Kang, L.; Du, B.; Zhao, H.; Xie, Q.; Huang, X.; Li, B.; Zhou, J.; Li, L. Experimental Demonstration of Isotropic Negative Permeability in a Three-Dimensional Dielectric Composite. *Phys. Rev. Lett.* **2008**, *101*, 027402.
24. Zhao, Q.; Zhou, J.; Zhang, F.; Lippens, D. Mie Resonance-Based Dielectric Metamaterials. *Mater. Today* **2009**, *12*, 60–69.
25. Evlyukhin, A. B.; Novikov, S. M.; Zywietz, U.; Eriksen, R. L.; Reinhardt, C.; Bozhevolnyi, S. I.; Chichkov, B. N. Demonstration of Magnetic Dipole Resonances of Dielectric Nanospheres in the Visible Region. *Nano Lett.* **2012**, *12*, 3749–3755.
26. Schmidt, M. K.; Esteban, R.; Sáenz, J. J.; Suárez-Lacalle, I.; Mackowski, S.; Aizpurua, J. Dielectric Antennas—A Suitable Platform for Controlling Magnetic Dipolar Emission. *Opt. Express* **2012**, *20*, 13636–13650.
27. Kuznetsov, A. I.; Miroshnichenko, A. E.; Fu, Y. H.; Zhang, J. B.; Luk'yanchuk, B. Magnetic Light. *Sci. Rep.* **2012**, *2*, 492.
28. Coenen, T.; Vesseur, E. J. R.; Polman, A. Angle-Resolved Cathodoluminescence Spectroscopy. *Appl. Phys. Lett.* **2011**, *99*, 143103.
29. Coenen, T.; Vesseur, E. J. R.; Polman, A.; Koenderink, A. F. Directional Emission from Plasmonic Yagi-Uda Antennas Probed by Angle-Resolved Cathodoluminescence Spectroscopy. *Nano Lett.* **2011**, *11*, 3779–3784.
30. Coenen, T.; Polman, A. Polarization-Sensitive Cathodoluminescence Fourier Microscopy. *Opt. Express* **2012**, *20*, 18679–19691.
31. García de Abajo, F. J. Optical Excitations in Electron Microscopy. *Rev. Mod. Phys.* **2010**, *82*, 209–275.
32. Sapienza, R.; Coenen, T.; Renger, J.; Kuttge, M.; van Hulst, N. F.; Polman, A. Deep-Subwavelength Imaging of the Modal Dispersion of Light. *Nat. Mater.* **2012**, *11*, 781–787.
33. Stevens-Kalceff, M. A. Cathodoluminescence Microcharacterization of the Defect Structure of Irradiated Hydrated and Anhydrous Fused Silicon Dioxide. *Phys. Rev. B* **1998**, *57*, 5674–5683.
34. *FDTD Solutions*; Lumerical Solutions, Inc.: Vancouver, BC, Canada; www.lumerical.com.

35. Palik, E. D. *Handbook of Optical Constants of Solids*; Academic: New York, 1985.
36. Jackson, J. D. *Classical Electrodynamics*; John Wiley & Sons: Hoboken, NJ, 1999.
37. Snyder, A. W.; Love, J. D. *Optical Waveguide Theory*; Chapman & Hall: London, 1996.
38. Slusher, R. E.; Levi, A. F. J.; Mohideen, U.; McCall, S. L.; Pearton, S. J.; Logan, R. A. Threshold Characteristics of Semiconductor Microdisk Lasers. *Appl. Phys. Lett.* **1993**, *63*, 1310–1312.
39. Kuttge, M.; García de Abajo, F. J.; Polman, A. Ultrasmall Mode Volume Plasmonic Nanodisk Resonators. *Nano Lett.* **2010**, *10*, 1537–1541.
40. Yu, Y.; Cao, L. Coupled Leaky Mode Theory for Light Absorption in 2D, 1D and 0D Semiconductor Nanostructures. *Opt. Express* **2012**, *20*, 13847–13856.
41. Yamamoto, N.; Ohtani, S.; García de Abajo, F. J. Gap and Mie Plasmons in Individual Silver Nanospheres near a Silver Surface. *Nano Lett.* **2011**, *11*, 91–95.
42. Vesseur, E. J. R.; Polman, A. Plasmonic Whispering Gallery Cavities as Optical Nanoantennas. *Nano Lett.* **2011**, *11*, 5524–5530.
43. Novotny, L.; Hecht, B. *Principles of Nano-Optics*; Cambridge University Press: New York, 2006.
44. Kuttge, M.; Vesseur, E. J. R.; Koenderink, A. F.; Lezec, H. J.; Atwater, H. A.; García de Abajo, F. J.; Polman, A. Local Density of States, Spectrum, and Far-Field Interference of Surface Plasmon Polaritons Probed by Cathodoluminescence. *Phys. Rev. B* **2009**, *79*, 113405.